Surface & Coatings Technology 484 (2024) 130767

Contents lists available at ScienceDirect

Surface & Coatings Technology

journal homepage: www.elsevier.com/locate/surfcoat

Full Length Article

Temperature-relevant degradation in amorphous carbon coated SS316L bipolar plates for PEMFC

Chao Jin [a,b], Peng Guo [b,**], Hao Li [b], Zhongyu Piao [a], Keiji Komatsu [d], Guanshui Ma [b], Rende Chen [b], Hidetoshi Saito [b,d], Aiying Wang [b,c,*]

[a] College of Mechanical Engineering, Zhejiang University of Technology, Hangzhou 310000, Zhejiang, PR China
[b] Key Laboratory of Advanced Marine Materials, Ningbo Institute of Materials Technology and Engineering, Chinese Academy of Sciences, 315201 Ningbo, PR China
[c] Center of Materials Science and Optoelectronics Engineering, University of Chinese Academy of Sciences, 100049 Beijing, PR China
[d] Graduate School of Engineering, Nagaoka University of Technology, 940-2188 Nagaoka, Japan

ARTICLE INFO

Keywords:
PEMFC
Amorphous carbon coating
Metal bipolar plates
Temperature
Corrosion resistance

ABSTRACT

The corrosion of metallic Bipolar Plates (BPs) has become a key bottleneck in the practical application of proton exchange membrane fuel cells (PEMFCs). Environmental factors inside the PEMFCs significantly accelerate the degradation of electrical conductivity and durability of metallic BPs. In this work, we investigated the corrosion behavior and conductive properties of amorphous carbon coating (a-C) coated SS316L in a simulated PEMFC environment at various operating temperatures. The results showed that the corrosion current density (I_{corr}) of a-C varied in a range of 2.3–8.7 nA/cm^2 when subjected to a temperature range of 40–80 °C. Additionally, the interfacial contact resistance increased from 4.36 to 9.56 mΩ/cm^2 with a rise in temperature. The reasons could be ascribed to two aspects. First, the a-C maintained the good chemical stability of sp^2/sp^3 bonds regardless of temperature changes, favoring remarkable anti-corrosion and good conductivity. Second, the higher temperatures intensified the penetration of corrosive species, accelerating the dissolution process of a-C coated SS316L and leading to substantial corrosion failure.

1. Introduction

Due to the remarkable combination of high energy density, large power efficiency, low-temperature operation as well as low emissions, the proton exchange membrane fuel cells (PEMFCs) have gained the increasingly attention as one of the most eco-friendly and popular fuel cell technologies [1–4]. However, the key practical bottlenecks for PEMFCs are the severe corrosive damage and easy dissolution of metallic bipolar plates (BPs) under harsh acidic media [5,6], which could significantly degrade the output power and lifetime of the PEMFC systems. Different with the traditional nitride and carbide ceramic coatings, amorphous carbon coatings (a-C) enable both strong corrosion resistance and high electrical conductivity for metallic BPs in PEMFCs [7–9]. The exceptional benefits of a-C coatings include high hardness, outstanding chemical inertness to acidic and alkaline solution, controlled electrical conductivity and facile low-temperature deposition with large uniformity for mass productions. The evident observations were that the commercialization of amorphous carbon-coated metallic BPs had been successfully attempted for fuel cell vehicles by various well-known automakers, such as Toyota and Mercedes-Benz [10,11].

Based on the US Department of Energy standardization (DOE-2025), recently, it is becoming a great challenge to improve the performance durability of a-C coated metallic BPs that require long-life service for PEMFCs. In particular, if one considers the running parameter coupled harsh acid solution used for practical PEMFCs, most of studies relevant to the single working condition is not sufficient to simulate the protective performance of coatings and thereafter to identify the corrosion failure accompanying with conductivity increment during actual process [12–14]. For instance, the potential changes distinctly within start-up/shutdown or transient stage, which would generate the highly temporary potential and strongly accelerate the corrosion of coated metallic BPs [15,16]. Compared to the pristine coating, the ICR value of a-C coated 316 L sample increased almost 5 times after potentiostatic test at 1.6 V [17]. In addition, the variety in pH value also affected the

* Correspondence to: A. Wang, Key Laboratory of Advanced Marine Materials, Ningbo Institute of Materials Technology and Engineering, Chinese Academy of Sciences, 315201 Ningbo, PR China.
** Corresponding author.
E-mail addresses: guopeng@nimte.ac.cn (P. Guo), aywang@nimte.ac.cn (A. Wang).

https://doi.org/10.1016/j.surfcoat.2024.130767
Received 6 March 2024; Received in revised form 29 March 2024; Accepted 6 April 2024
Available online 9 April 2024
0257-8972/© 2024 Elsevier B.V. All rights reserved.

corrosion behavior of the metallic BPs [18,19]. The evidence could be observed that, with increase of acidity, a longer time ranging from 1900 to 4700 s was required for SS304 to reach the steady state, accompanying with the increase of stabilized corrosion current density (I_{corr}) from 0.043 to 0.547 μA/cm^2 [20]. Furthermore, by utilizing a double cell device consisted of one side for hydrogen charging and another side for electrochemical test, Wang et al. [21] found that the presence of hydrogen improved I_{corr} approximately four times larger than that without hydrogen, indicating the positive influence of hydrogen during running process of PEMFCs.

Beyond of the above mentioned issues, another key concern would be the temperature situation within PEMFC stacks, which could also affected by current distribution [22], relative humidity [23], reactant gas partial pressure [23], working gas flow rate [24] and running time [22–24] during practical applications. An indication was that the stable corrosion current density of SS316L was improved almost 5 times as the temperature increased from 25 to 90 °C in a simulated PEMFC environment [25]. Similar results were reported by Xuan et al. [26], where the corrosion current density of SS304 even increased about 6 times from 25 to 80 °C together with the severe degradation of ICR after 5 h potentiostatic polarization at 0.6 V. In this case, it could be very importance to clarify the dependence of corrosion behavior and conductivity for a-C coated metallic BPs, especially because of the versatile features in a-C families and the complex characteristics in hybridized atomic bonds of carbon materials.

In our previous paper, we successfully prepared a-C coating with high conductive and corrosion-resistant properties, and investigated the protective behavior on SS316L. The results showed that enhancing the density of a-C coating was crucial for prolonging its durability in harsh environments [27,28]. Nevertheless, it is still far lack of study on the dependence of electrochemical behavior upon the running environmental factors for the a-C coated BPs. In this study, the optimized a-C coating was specifically deposited on SS316L substrate by a hybrid direct current magnetron sputtering technique. The focus was dedicated to the understanding between corrosion resistance and electric conductivity of a-C coating samples in the simulated PEMFCs condition with controlled operating temperature from 40 °C to 80 °C. The electrochemical property and ICR were comprehensively discussed in terms of the structural evolutions, which were deduced from surface morphology, microstructure and atomic bonds after long-term corrosion test. The work can provide valuable guidance for the designing and developing of commercialized a-C coated metallic BPs in PEMFCs and the insights into failure mechanism during long-time operating.

2. Experimental procedure

2.1. Sample preparation

The SS316L substrates were ground and polished using SiC abrasive paste (HY401-J), subsequently following the cleaning process with acetone and alcohol solution in an ultrasonic bath for 30 min. After the wild cleaning, the substrates were installed on a rotation jig-holder in the vacuum chamber. The a-C coatings were deposited on substrate by a hybrid direct current magnetron sputtering (DCMS) technique, where a rectangular graphite target (size of 400 mm × 100 mm × 7 mm, purity of 99.99 wt%) and a chromium target with same dimension and purity was applied as carbon and chromium ions source, respectively. Fig. 1 shows the schematic diagram of deposition system for a-C synthesis. Before deposition, the substrates were etched by Ar^+ ions using glow discharge at a DC pulsed bias of −600 V for 30 min, in order to remove the surface contaminants and improve the adhesion strength of coating/substrate. When the base pressure of chamber was evacuated down to 2×10^{-3} Pa, a dense chromium buffer-layer with 100 nm was fabricated by high-power impulse magnetron sputtering (HiPIMS) to enhance the coating adhesion under a DC pulsed substrate bias of −50 V, in which the pulse width and frequency was set at 100 μs and 500 Hz. Next, 200 nm-thick a-C coating as top layer was synthesized by DCMS method with a supplied substrate bias of -50 V, and the sputtering power for carbon source was around 2 kW. More experimental details could be referred to our previous reports [27,28]. Noted that, beyond of SS316L substrate, the p-

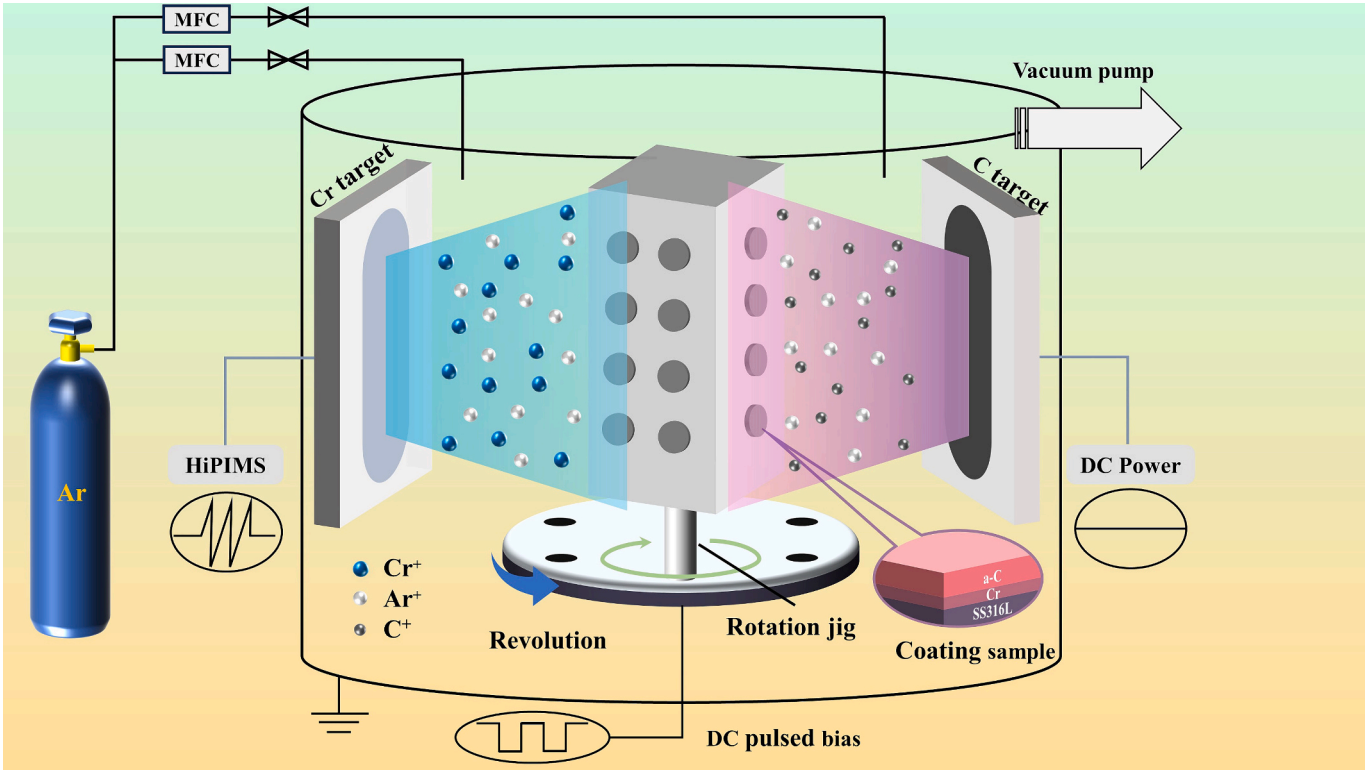

Fig. 1. The schematic diagram of hybrid deposition system for coating synthesis.

type (100) crystalline Si wafer was also used as substrate for easier measurement of coating surface and cross-section morphology comparatively.

2.2. Morphology and composition analysis

The surface and cross-sectional morphologies of the coating were characterized using a field-emission scanning electron microscopy (FESEM, Verios G4 UC, USA) equipped with an energy dispersive X-ray spectrometer (EDS, Oxford, UK) at a voltage of 15 kV. After corrosion tests at different temperatures, the composition of the passive coating on SS316L, as well as the composition and atom binding state of the a-C coating after corrosion tests at different temperatures were elucidated using the X-ray photoelectron spectroscopy (XPS, Axis Ultra DLD, Japan) with an Al Kα X-ray source (1486.6 eV). For the XPS depth profile, the surface was sputtered by Ar^+ ion bombardment using an ion beam of 2 kV. The C1s peak (284.8 eV) was used as a reference to correct the standard electron binding energies for all XPS peaks, where the XPS data were analyzed using the CaseXPS software. The microstructure of the a-C coating before and after corrosion was characterized using high-resolution transmission electron microscopy (HRTEM, Tecnai F20, USA).

2.3. Electrochemical measurements

The Gamry electrochemical workstation (Reference 600+, US) was employed to measure the electrochemical behavior of the coatings, where a traditional three-electrode system was especially operated. Particular, the Ag/AgCl electrode acted as the reference electrode, the platinum sheet was used as the counter electrode, while the test sample performed like a working electrode. To simulate the actual PEMFC operating environment, all the samples were immersed into the 0.5Mol H_2SO_4 + 5 ppm HF mixed solutions under various running temperatures (40 °C, 60 °C, and 80 °C). Before the electrochemical corrosion tests, the specimens were put in the solutions with an open circuit potential (OCP) for 2 h to reach a steady-state potential. Then the potentiodynamic polarization was conducted from −0.2 V vs. Ag/AgCl ranging to +1.2 V vs. Ag/AgCl with a scanning rate of 0.5 mV/s. Electrochemical impedance spectroscopy (EIS) was carried out in the frequency range from 10^5 to 10^{-2} Hz with a disturbing AC amplitude of 10 mV. Furthermore, the EIS spectra were analyzed and fitted by the ZSimpWin software to gain informative characteristics. Under the simulated PEMFC cathode running situation, the long-time potentiostatic test was performed at 0.6 V vs. Ag/AgCl for the purpose of evaluating the durable life of a-C coating modified SS316L plates. After 12 h and 24 h potentiostatic tests, the acid solution was specifically collected and analyzed by inductively coupled plasma–optical emission spectrometer (ICP-OES). According to the analysis, the concentrations of released chromium and iron ions after electrochemical tests could thereafter be determined [29,30]. In addition, the Mott-Schottky tests were employed to identify the characteristic of charged species in the potential range from −0.2 V to 1.0 V and DC steps was 10 mV.

2.4. Conductivity measurements

During the ICR test, two pieces of conductive carbon paper (Toray TGP-H-060) were firstly sandwiched between the specimens and two gold-coated copper plates. A constant electrical current at 1 A was introduced via the two copper plates under test procedure, and the variety of the total voltage was recorded by a precision multimeter. The external pressure was supplied to the integrated plates and identified by the universal testing machine (2 kN, Chine). The resistance of circuit was calculated using voltammetry. The ICR test was repeated at least three times to get the average value, where the representative ICR position was selected at load of 1.38Mpa according to the DOE-2025 standardization. More details for ICR measurement could be found in the literature [31].

3. Result and discussion

3.1. Surface and cross-sectional morphology of a-C coating

Fig. 2 shows the cross-sectional image and top-view SEM morphology of a-C coating deposited on typical Si substrate. It was obvious that the thickness of Cr buffer-layer was about 100 nm, while the top-layer a-C coating exhibited a thickness of 200 nm (Fig. 2a). In addition, both the a-C/Cr interface and Cr/SS316L interface were pretty clear, demonstrating free of distinct voids or defects in multilayer structure. As shown in Fig. 2b, the a-C coating combined Cr buffer-layer indicated the smooth and dense surface, even the obscure cauliflower-like structure with an average size around 60 nm was visible from the inserted image with magnification. In general, the a-C coating possessed the typical amorphous characteristics, this observation of cauliflower-like structure could be arisen from the columnar growth of the Cr coating layer adjacent to a-C layer. However, it was noticeable that introducing HiPIMS process significantly enabled the densely columnar growth and crystalline refinement for Cr deposition compared to the other reports [32].

3.2. Potentiodynamic polarization results

The potentiodynamic polarization curve of SS316L without and with a-C coating is shown in Fig. 3a–b for comparison. Both two samples exhibited the similar polarization behavior, as evidenced by the absence of an active current peak on the polarization curves. However, it was clear that the I_{corr} for both samples shifted upward as the temperature increased, indicating that temperature accelerated the anodic reaction. Furthermore, at the equivalent operating temperature, the a-C coated SS316L reduced the I_{corr} about 2 orders of magnitude than that of uncoated one due to the promising corrosion resistance of a-C coating. As the potential increased, the anode curves of two samples exhibited different trends. When the potential exceeded 0.9 V, the I_{corr} sharply increased for SS316L, suggesting the occurrence of trans-passivation at high potentials [20]. In contrast, the I_{corr} increased at a slow tendency for a-C case. With the typical simulated operating potential of 0.6 V in the cathodic environment of PEMFCs, the I_{corr} in a-C coated SS316L was measured to be 3.4, 4.1, and 3.5 nA/cm^2 at temperature of 40 °C, 60 °C and 80 °C, respectively, which were all pretty satisfied with the DOE 2025 standard value of 1 μA/cm^2.

3.3. Potentiostatic polarization measurements

To assess the long-term corrosion resistance of bare SS316L and a-C coated SS316L, Fig. 4 shows the potentiostatic polarization tests with 24 h conducted at 0.6 V. The I_{corr} in both SS316L and a-C coated samples exhibited a continuous downward trend initially, and substantially reaching to the stable level. For comparison, the a-C coated SS316L achieved a steady state more quickly, and the stable I_{corr} was at least one order of magnitude lower than that of SS316L. This revealed that the electrochemical reactions were intensively suppressed in the a-C coated SS316L. At 80 °C, all the curves for two sample fluctuated with presence of abrupt spikes, indicating the occurrence of localized pitting corrosion. Fig. 4c presents that the stabilized I_{corr} for both SS316L and a-C coated SS316L. The stable I_{corr} of a-C coated SS316L was 2.3, 4.7, and 8.7 nA/cm^2, respectively, which were lower than the I_{corr} of SS316L. The results indicate that the a-C coating effectively enhances the ability of SS316L to resist corrosion in the fluctuating temperatures of PEMFCs.

3.4. Dissolution of metal ions

Released metal ions are pivotal parameters in evaluating the extent of damage to metallic BPs [31]. The corrosion solutions were collected

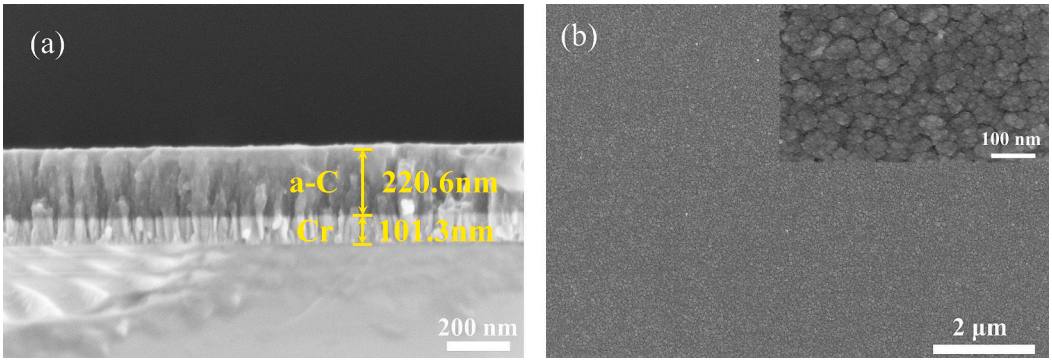

Fig. 2. The cross-sectional (a) and top-view (b) SEM images of a-C coating combined with Cr buffer-layer deposited on Si substrate.

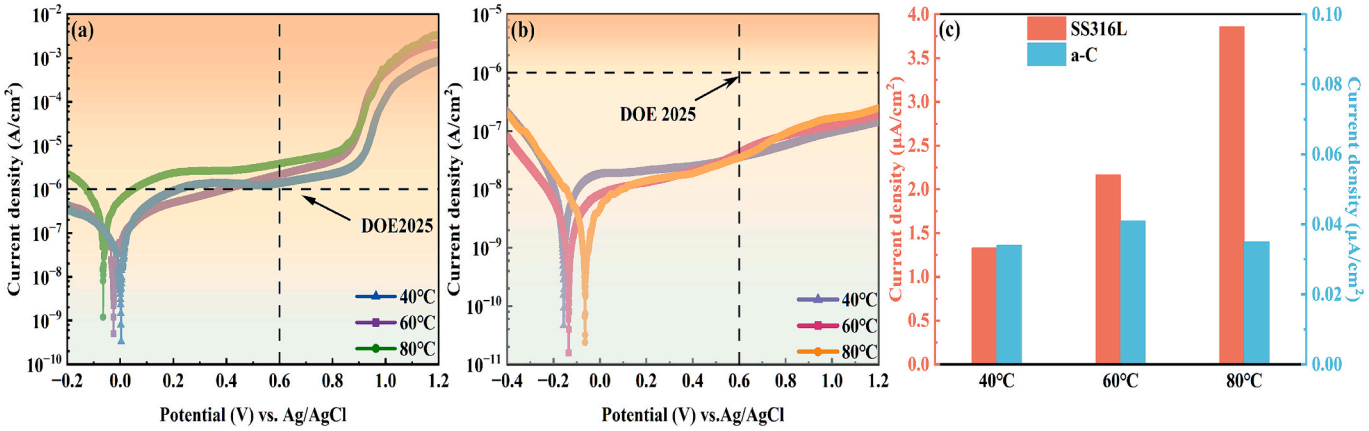

Fig. 3. Potentiodynamic polarization curves of SS316L (a) and coated samples (b) under different temperatures; the corrosion current densities of SS316L and coated samples at 0.6 V (c).

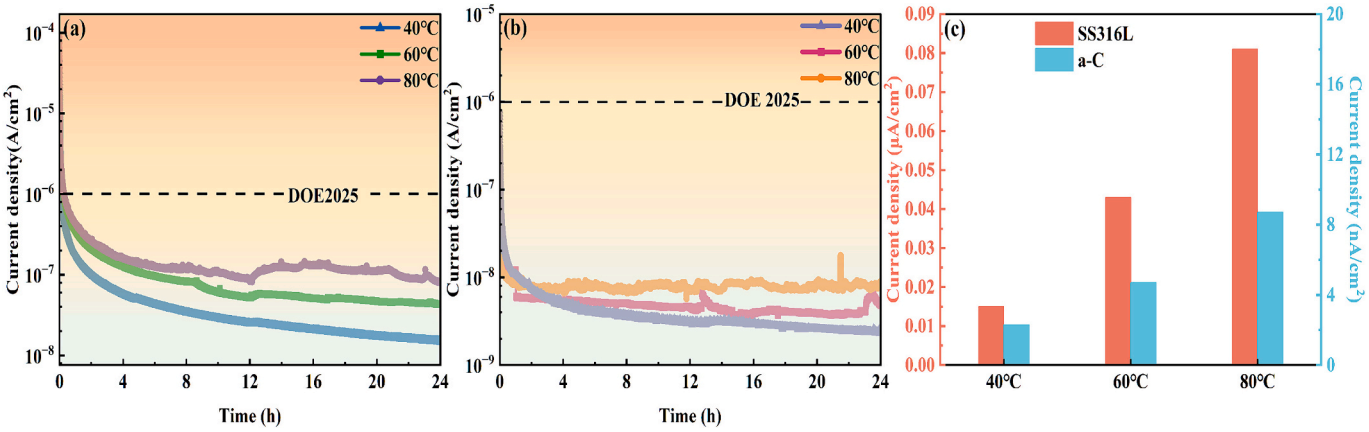

Fig. 4. Potentiostatic polarization curves of SS316L (a) and coated samples (b) under different temperatures; (c) the stable corrosion densities of SS316L and coated samples.

after 12 h and 24 h potentiostatic polarization tests, and the concentrations of primary metal ions mainly originated from Cr and Fe are summarized in Table 1. Obviously, the concentrations of Fe and Cr ions increased significantly with prolonging test durations and operating temperatures. In the case of SS316L samples, the concentrations of Fe and Cr ions demonstrated a nearly linear escalation with the rise in temperature over the same duration, where the maximum values of 0.35 ppm and 1.54 ppm was achieved at 80 °C, respectively. However, in contrast to SS316L, both the concentrations of Cr and Fe ions were extensively reduced in a-C-coated SS316L, being close to zero at temperatures below 60 °C, even the relevant ionic concentrations were accelerated greatly at 80 °C. Based on this observation, it could be suggested that higher operating temperature could accelerate the corrosion of metallic bipolar plates and a-C coating to a great extent, while the a-C coating still inhibited the ions releasement from SS316L substrate comparatively.

3.5. EIS analysis

Fig. 5 presents the Nyquist and Bode plots of SS316L and a-C coated

Table 1
The released metal ions of SS316L and a-C coated SS316L after 12 h and 24 h potentiostatic polarization under different temperatures.

Samples	Temperature	Released metal ions/h			
		Cr-12 h	Cr-24 h	Fe-12 h	Fe-24 h
SS316L	40 °C	0.073	0.098	0.194	0.239
	60 °C	0.132	0.171	0.440	0.590
	80 °C	0.290	0.350	1.220	1.540
a-C	40 °C	0.013	0.014	0.093	0.118
	60 °C	0.017	0.028	0.125	0.180
	80 °C	0.101	0.117	0.507	0.695

SS316L in a 0.5 M H_2SO_4 + 5 ppm HF mixed solution at different temperatures. After analyzing the Nyquist curves in Fig. 5a for SS316L, increasing temperature led to an obvious reduction in the diameters of capacitive loops, indicating the exacerbated corrosion of the metallic BPs. In the Bode diagrams (Fig. 5b), the impedance moduli consistently decreased at low frequency with temperature ascending, accompanied by a corresponding drop in phase angle. The Bode phase angle diagrams exhibited a peak resulting from capacitance response in the range of low and intermediate frequency. Especially, the presence of a low-frequency capacitive region evidenced the corrosion solution originated from substrate or chromium buffer-layer, where the electrochemical reactions were triggered at the interface [33]. Taking the analysis of Fig. 5b, an equivalent circuit evolving two time constants (inserted in Fig. 5a) was used for the fitting of EIS data.

Fig. 5c displays Nyquist plots for the a-C coated SS316L. In contrast to bare SS316L substrate, there was the semi-circle diameters expanded for the a-C coated SS316L sample, indicating the enhanced corrosion resistance. The relevant Bode plots (Fig. 5d) revealed a wider phase angle plateau and higher low-impedance moduli compared to SS316L, evidencing the superior capacitive behavior as well. Significantly, the impedance moduli of a-C coating exhibited near-zero variation in temperature range of 40–80 °C, confirming the excellent chemical stability of a-C coating.

Nevertheless, if one regarded the data shown in Table 1, a small amount of metal ions was still presented in the corrosion solution for a-C coated sample. This proposed the permeation of the corrosive species through a-C matrix, causing the corrosion of SS316L substrate. Thanks to the chemical stability of a-C coating, it could be assumed there was a passive layer formed on the SS316L, akin to the substrate's condition. Thereafter, same equivalent circuit model shown in inserted Fig. 5a was suitable for EIS fitting in a-C coated case. Considering the concentration

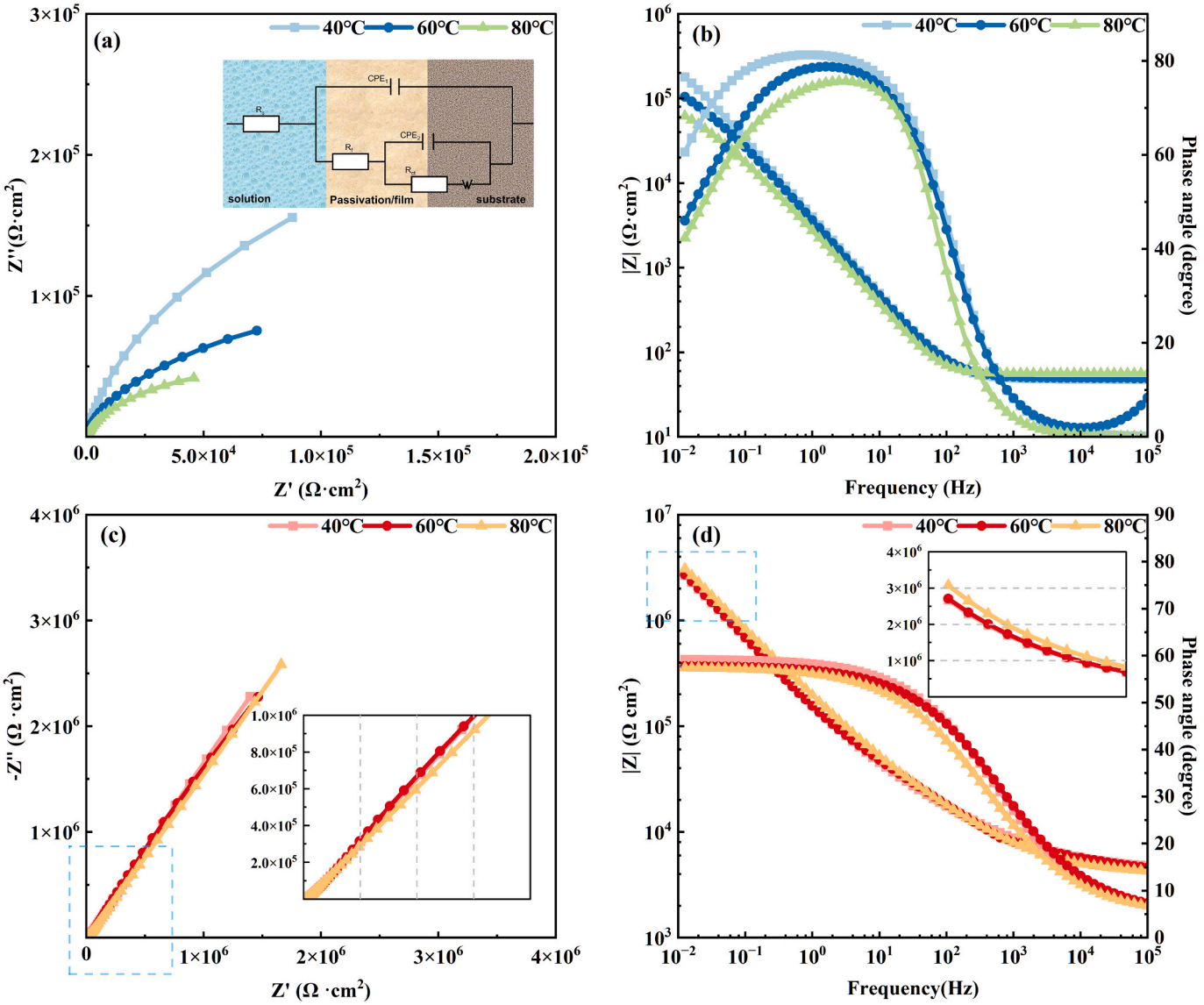

Fig. 5. Electrochemical impedance spectroscopy of SS316L (a, b) and a-C coated samples (c, d) under different temperatures: Nyquist curves (a, c), Bode plots (b, d).

polarization and dispersion effect, the constant phase element (CPE) and Warburg impedance (W) were introduced [34]. The impedance of the Z_{CPE} could be acquired by the following equation [33]:

$$Z_{CPE} = [Y_0(j2\pi f)^n]^{-1} \quad (1)$$

where j is $-1^{0.5}$, f is the frequency, Y_0 is the magnitude of CPE and n is the parameter related to the CPE. In this circuit model, R_s represents the solution resistance, CPE_1 and R_f denote the capacitance and resistance of the protective coating, respectively. CPE_2 and R_{ct} stand for the capacitance of the double electrical layer and the charge transfer resistance at the coating/substrate interface.

Table 2 shows the fitting parameters obtained from the EIS data. The R_f exhibited a decrease with escalating solution temperature, indicating a continuous reduction in the resistance of the protective layers for both SS316L and a-C coated samples. Under identical temperatures, the R_f of a-C coated samples surpassed that of SS316L by one order of magnitude, evidencing the significant deceleration of the corrosion process facilitated by the a-C coating. Generally, the protective efficacy of the formed passive coating or deposited coatings could be evaluated through the R_{ct} value, where a higher R_{ct} signified the improvement of corrosive resistance to ion diffusion [35,36]. It could be observed that, comparing with the R_{ct} of SS316L, a-C coating behaved the two orders of magnitude increase, indicating superior resistance to corrosive ion diffusion and strongly protective capability. In particular, the highest R_{ct} value for the a-C coated sample about 6.246×10^7 Ω·cm^2 was observed at 40 °C, while the lowest R_{ct} data of 2.309×10^6 Ω·cm^2 was recorded at 80 °C. The decline in R_{ct} suggested that higher temperature greatly sacrificed the protection performance of the a-C coating.

3.6. Mott-Schottky study on the SS316L

In order to address the semiconductor characteristic of the formed passive film on SS316L and a-C coated SS316L, we conducted the Mott-Schottky test. It was empirically known that the correlation between the applied potential and the capacitance could be described by the Mott-Schottky equation, as follows [37–39]:

For n-type semiconductor

$$C^{-2} = \frac{2}{\varepsilon\varepsilon_0 e N_A}\left(E - E_{FB} - \frac{KT}{e}\right) \quad (2)$$

And for p-type semiconductor

$$C^{-2} = -\frac{2}{\varepsilon\varepsilon_0 e N_A}\left(E - E_{FB} - \frac{KT}{e}\right) \quad (3)$$

where C is the capacitance of the space-charge layer (F·cm^2), N_D and N_A are the donor and acceptor densities, respectively. While ε is the dielectric constant of the passive coating (0.156 F/cm^2) [40]. ε_0 is the vacuum dielectric constant (8.854×10^{-14} F/cm^2), e is the electronic charge about 1.602×10^{-19}C, E is the potential, E_{fb} denotes the flat band potential, k is the Boltzmann's constant (1.38×10^{-23} J/K) and T is the absolute temperature.

Fig. 6a shows the Mott-Schottky curves of SS316L after 24 h polarization in a simulated PEMFC cathode environment at 0.6 V. The plot delineated two regions based on the positive or negative slope. A positive slope between 0.1 and 0.6 V demonstrated the electronic behavior of an n -type semiconductor. Beyond of 0.6 V, the curve's slope turned to negative, signifying a transition from n-type to p-type semiconductor characteristics. The variation in slope with applied potential might commonly be attributed to the duplex structure and composition of the passive coating on SS316L [41–44]. Fig. 6b illustrates the Mott-Schottky plots of the a-C coated SS316L, which display linear relationship between $1/C^2$ and E with positive slopes, suggesting its n-type semiconductor character.

Table 3 presents the fitted donor and acceptor densities, as well as the flat band potential. It was observed that all the value of N_D, N_A and E_{fb} exhibited an increasing trend with rising temperature. This increment became more pronounced as the solution temperature elevated from 60 °C to 80 °C than those in range of 40–60 °C. According to the point defect model (PDM) [31,45], elevated temperatures could easily lead to higher rates of oxygen vacancies and anion interstitials generation at the interface between metal/coating, expediting the elimination at the coating/solution interface. Furthermore, if the accumulation exceeded the destruction, point defects would accumulate within the passive coating, resulting in the increase of carrier densities [46]. The higher carrier density indicated a greater probability of breakdown and pitting corrosion in the passive coating. The carrier density of the a-C coated SS316L is obviously lower than that of SS316L, indicating that the a-C coating reduced vacancy type structural defects, which is conducive to restraining the penetration of corrosive ions and improving the corrosion resistance.

3.7. Surface morphology after the electrochemical tests

Fig. 7 illustrates the surface morphology and elemental distribution of SS316L and a-C coated SS316L after 24 h potentiostatic polarization. As shown in Fig. 7a–c, the number and size of corrosive sites on the SS316L surface noticeably increased with the increase of solution temperature. Especially at 80 °C, the corrosion pits with large-size of 75 μm emerged on the surface of SS316L (Fig. 7c) following polarization. Additionally, an accumulation of oxygen element was achieved in this area, demonstrating the severe localized corrosion. In contrast, the a-C coated SS316L exhibited an absence of apparent corrosive pits and reactive dissolution even at the given temperatures (Fig. 7d–f), evidencing the a-C coating could provide better corrosion resistance and stability to the metallic BPs regardless of the temperature changes in the PEMFCs.

3.8. XPS analysis

Fig. 8a–c presents the distribution of O, Ni, Fe and Cr elements on the SS316L after 24 h potentiostatic polarization. Analyzing the variety in typical Cr and Ni element shown in Fig. 8a–c, the depth profiles under different temperatures showed the similar tendency, which were

Table 2
Fitting data of EIS results of SS316L and a-C coated SS316L under different temperature.

Samples	Temperature	Rs (Ω·cm^2)	CPE_1		R_f (Ω·cm^2)	CPE_2		Rct (Ω·cm^2)	W (Ω·S$^{0.5}$·cm^2)
			Q_1 (Ω^{-1} cm^{-2} S^n)	n		Q_2 (Ω^{-1} cm^{-2} S^n)	n		
SS316L	40 °C	10.8	4.645×10^{-5}	0.970	148	9.80×10^{-5}	0.871	3.686×10^5	3.192×10^{-4}
	60 °C	4.96	3.875×10^{-5}	0.917	95.45	6.61×10^{-5}	0.800	1.484×10^5	1.651×10^{-4}
	80 °C	4.03	2.605×10^{-5}	0.945	14.49	4.84×10^{-5}	0.719	9.542×10^4	1.891×10^{-4}
a-C	40 °C	19.72	1.683×10^{-6}	0.683	1340.1	6.261×10^{-6}	0.943	6.246×10^7	3.540×10^{-8}
	60 °C	15.87	1.094×10^{-6}	0.734	960.31	4.995×10^{-6}	0.899	4.268×10^7	3.190×10^{-8}
	80 °C	11.25	1.507×10^{-6}	0.770	640.64	5.615×10^{-6}	0.869	2.309×10^7	4.199×10^{-8}

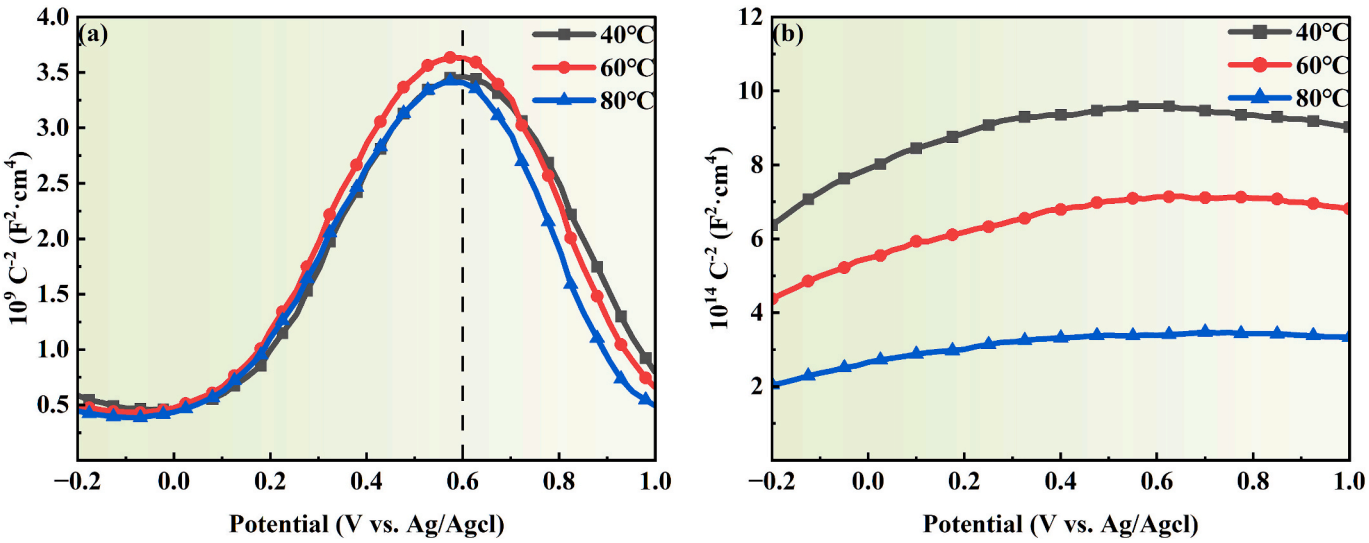

Fig. 6. The Mott-Schottky plots of SS316L (a) and a-C coated SS316L (b) after potentiostatic test (24 h, 0.6 V) with different temperatures of the solution (40 °C, 60 °C, and 80 °C).

Table 3
The donor densities, acceptor densities, and flat band of passive film on SS316L and a-C coated SS316L.

Samples	Elements	ND (cm^{-3})	NA (cm^{-3})	E_{fb} (V)
SS316L	40 °C	1.062×10^{21}	1.401×10^{21}	0.06
	60 °C	1.089×10^{21}	2.597×10^{21}	0.05
	80 °C	1.186×10^{21}	8.217×10^{21}	0.09
a-C	40 °C	7.513×10^{15}	\	−1.342
	60 °C	1.334×10^{16}	\	−1.129
	80 °C	3.226×10^{16}	\	−1.238

categorized into three regions: Region I, where the Cr/Ni content increased along the surface-to-bulk direction and reached its maximum value. The change in this region was regarded as initial place in the passive coating; Region II, where the Cr/Ni content gradually decreased from the maximum value; and Region III, where the Cr/Ni content was stabilized with detecting depth. As for the Fe content, it sharply increased in Region I and II, and gradually reached to a stable value in Region III.

Fig. 8d illustrates the Cr/Fe ratio with detection depth in the passive coatings. The Cr/Fe atomic ratios showed the highest value on the surface and continuously decreased from over 1.2 at the superficial layer to 0.2 around at the inner layer for each specimen. This phenomenon was

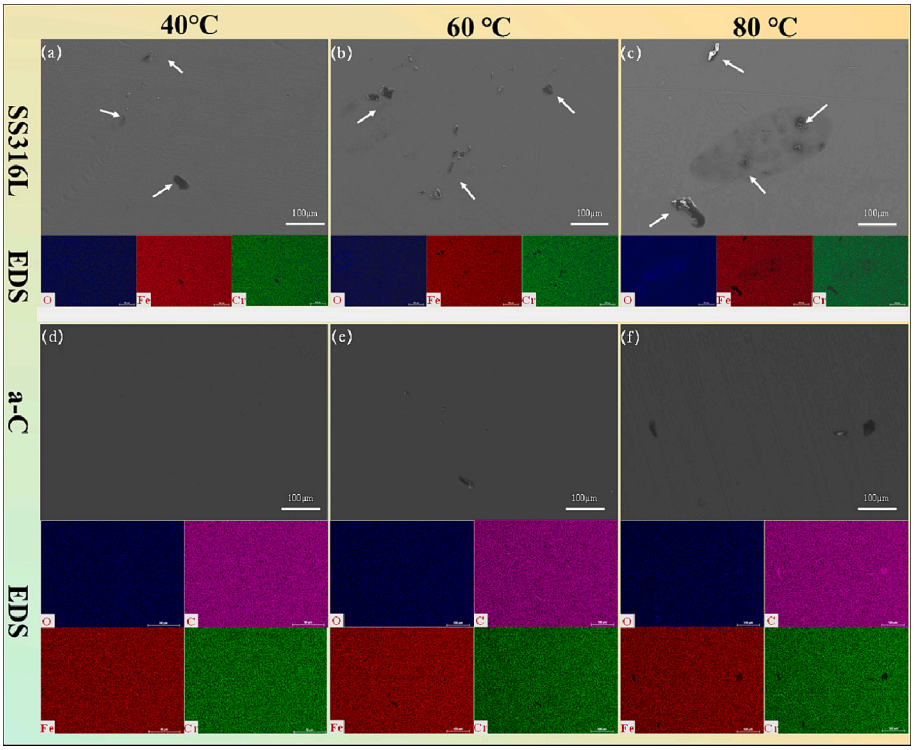

Fig. 7. SEM images and EDS results of SS316L (a–c) and a-C coated SS316L (d–f) after potentiostatic tests under different temperatures (40 °C, 60 °C, and 80 °C). The arrows point out some local corrosion spots.

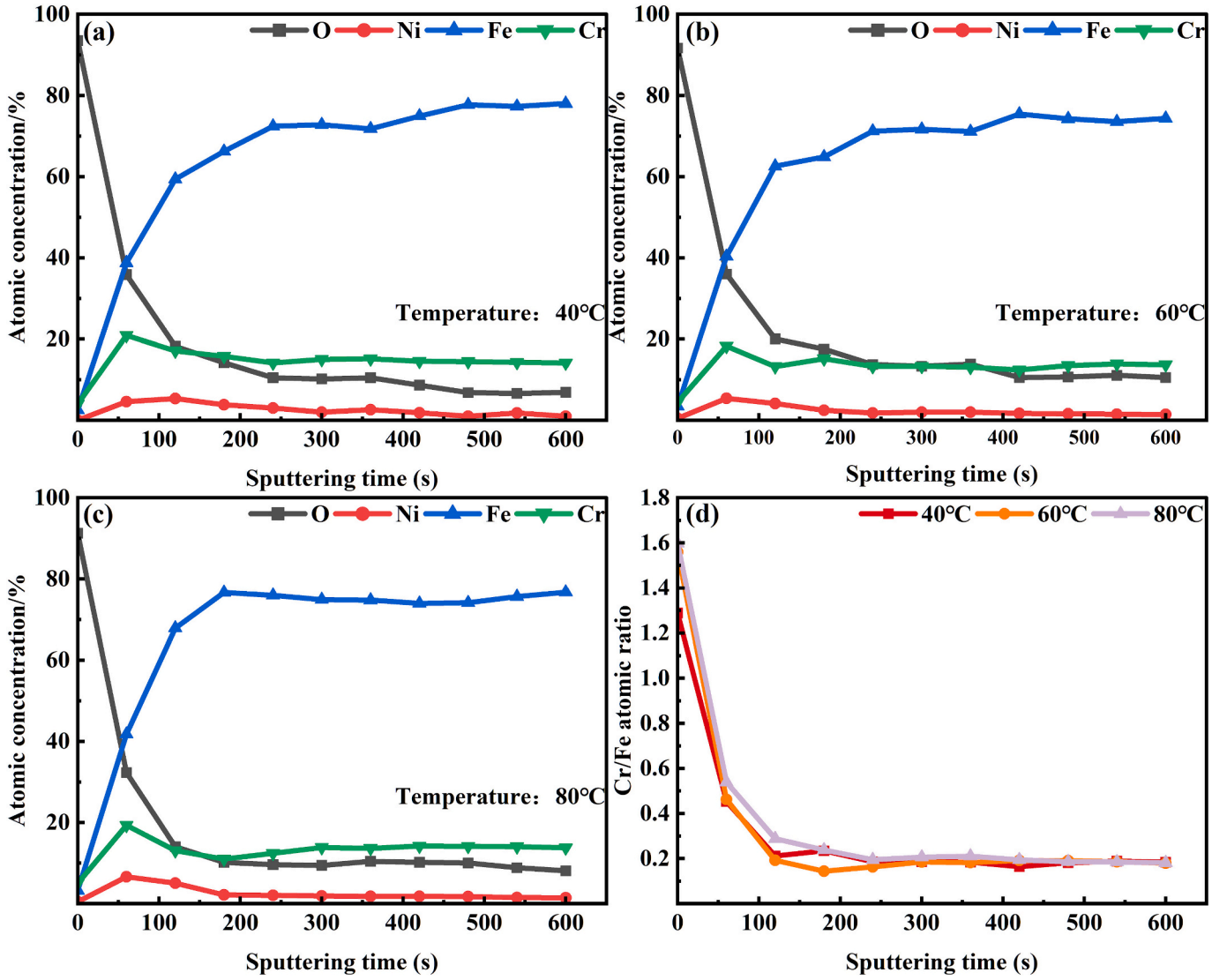

Fig. 8. The XPS depth profiles (a–c) and the Cr/Fe ratio with detection depth in the passive film formed on SS316L (d) after 24 h 0.6 V vs. Ag/AgCl polarization with different temperature.

primarily attributed to the easier dissolution of iron oxides compared to chromium oxides in the simulated solution, resulting in the highest Cr/Fe ratio on the surface [20,41,47]. Subsequently, the content of iron oxide went upwards sharply, illustrating a bi-layer structure in the passive coating, which might predominantly consist of iron oxide and chromium oxide.

Fig. 9 further shows the XPS C1s of the a-C coated samples before and after 24 h potentiostatic polarization. Since the C1s spectra could be deconvoluted into two peaks by fitting with 80 % Gaussian and 20 % Lorentzian function [48,49], the peak around 284.8 eV and 285.6 eV could be identified as sp^2-C and sp^3-C, respectively. Clearly, the as-deposited a-C exhibited a $sp^2/(sp^2 + sp^3)$ ratio of 55.8 % and few O atoms were detected, given the sample's exposure to the air before XPS test [50]. Following the electrochemical corrosion test, however, the $sp^2/(sp^2 + sp^3)$ ratio slightly decreased from 53.27 % to 48.49 % with increasing temperature from 40 to 80 °C. This decline might be attributed to the enhanced susceptibility of sp^2-C to corrosion in harsh acidic electrolytes [51].

Fig. 9b–d shows the distributions of C, O, Cr, and Fe elements across the a-C coated SS316L after a long-term polarization test at various temperatures. It was found that the oxygen content reached the maximum value, while the carbon content arrived the lowest level on the coating surface. As the sputtering time was increased, the oxygen content went downward, but the carbon content increased to a constant value, indicating the maintained good stability in chemical composition of a-C coating. Furthermore, traces of Cr and Fe elements were discovered in the coating, which deduced that the corrosion reaction primarily occurred on the SS316L substrate and the corrosion products could diffused from coating defects to its surface [52].

3.9. ICR analysis

With the increase of applied pressure, the ICR value of both SS316L and a-C coated SS316L continuously decreased (Fig. 10a). This phenomenon was mainly the consequence of the expansion in effective contact area between the test sample and carbon paper, thereby enhancing the channel of electron transmission. When the compression force exceeded 1 MPa, no significant decline was observed in ICR value. Nevertheless, after the durability tests, the ICR values of all test samples increased with both test temperature and time. As shown in Fig. 10b, the ICR of the bare SS316L was notably larger at 85.88 $m\Omega \cdot cm^2$ under 1.4 MPa (the typical stack compaction force for BPs), which could not meet well with the required value of DOE2025 (10 $m\Omega \cdot cm^2$). After potentiostatic test, the ICR further increased due to the generation of poorly

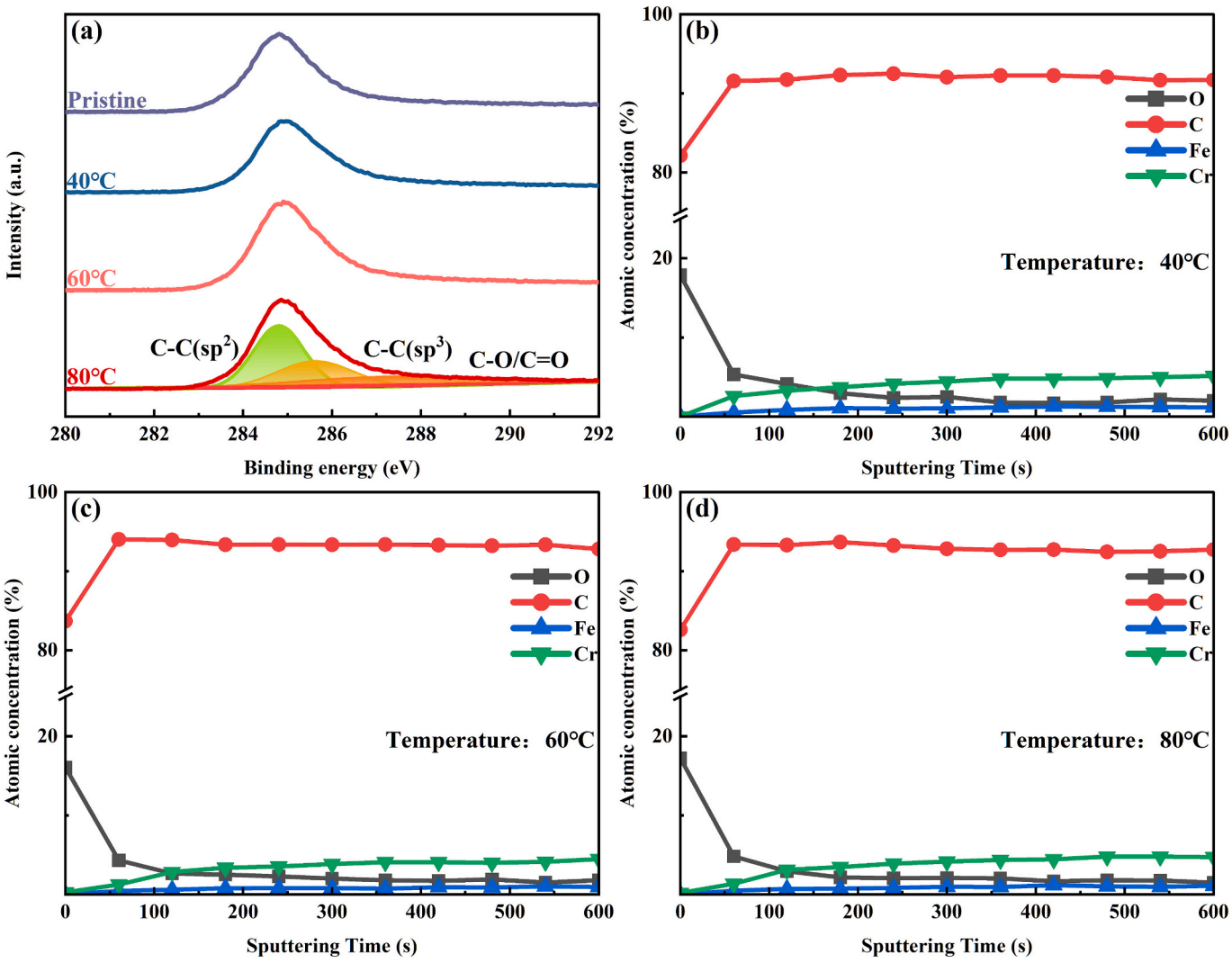

Fig. 9. The XPS spectra of C 1s (a) and XPS depth profiles (b–d) of the a-C coatings after 24 h polarization at different temperatures (40 °C, 60 °C, and 80 °C).

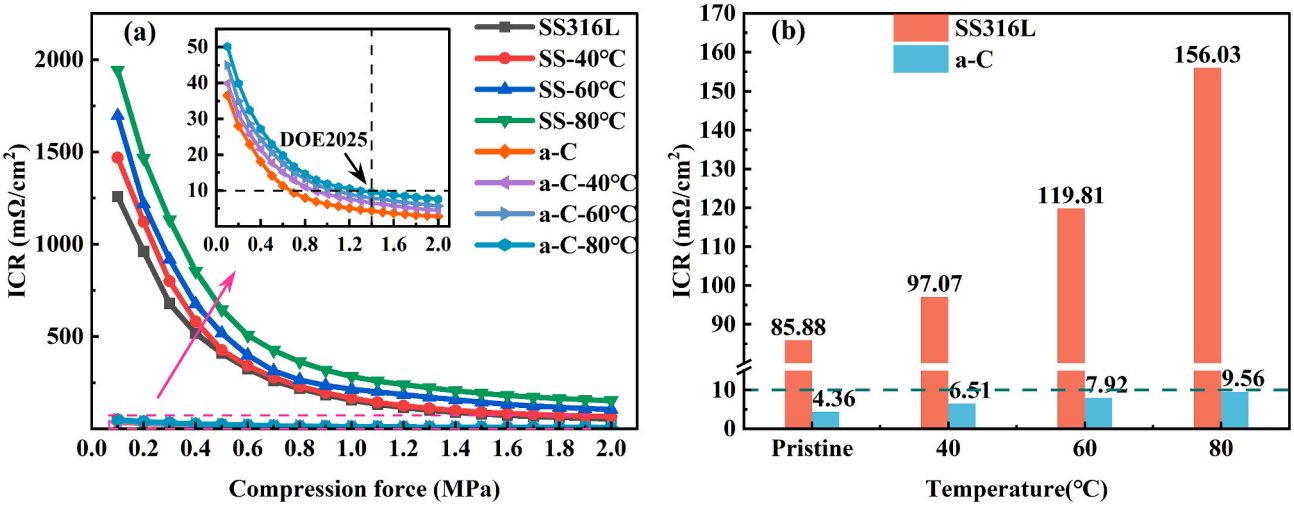

Fig. 10. The ICR of SS316L and a-C before and after the potentiostatic tests with different temperatures (40 °C, 60 °C, and 80 °C), (a) ICR at various compression forces, (b) ICR at 1.4 MPa.

conductive passive products on the SS316L surface. In comparison, a-C coated SS316L presented the ICR around only 4.36 mΩ·cm^2, which was slightly increased after the potentiostatic test. However, noted that such a deteriorated ICR was still within the value of DOE 2025 standardization. In could be thereafter concluded that the a-C coating significantly reduced the ICR together with enhancing the electrochemical performance of SS316L under PEMFC operating conditions.

3.10. Discussion on the role of test temperature

Based on the long-term corrosion test in Fig. 4, the I_{corr} of SS316L increased from 0.015 μA/cm^2 to 0.081 μA/cm^2 as the operating temperature ascended from 40 °C to 80 °C, evidencing a significant deterioration in the corrosion resistance of SS316L. The XPS analysis (Fig. 9) showed that the synergistic effect of metallic corrosion and the formed passive coating led to the performance degradation. Furthermore, according to the Mott-Schottky characterization, the carrier density of the passive coating increased abruptly with the temperature increment, resulting in a serious acceleration of the corrosion failure of SS316L substrate.

In contrast to SS316L, the a-C coated SS316L demonstrated the significant improvement of corrosion resistance (8.7 nA/cm^2), accompanying with the lowed ICR value of 4.36 mΩ·cm^2. The XPS analysis (Fig. 9) and the HRTEM (Fig. S1) results identified the stable structure of the a-C coating, which offered the remarkable protection even after the long-term polarization tests. Nevertheless, according to our previous work [28,33,52], there would be the existence of growth defects like pinholes and macroparticles formed in a-C coating during physical vapor deposition process, allowing corrosive electrolytes to penetrate the metallic substrate easily along these defects. This would be the key factor for the observed substrate corrosion at interface. Increasing temperature stimulated the corrosion sacrifice of a-C coated samples (Fig. 3), in which the higher Fe and Cr ions concentration (Table 1) and larger ICR value (Fig. 10) were observed as expected. Noticeably, it was likely that the corrosive ions such as H^+ and F^- possessed the more strongly active mobility and higher ionic diffusion at higher temperature [53–55]. Therefore, these corrosive species could easily reach to the interface through defects in the a-C coating and induced more severe corrosion of the substrate. Meanwhile, the emerged passive layer on the SS316L substrate owned the larger conductivity at high temperatures, as indicated by the Mott-Schottky test (Fig. 6), which might in turn accelerate the corrosion at the interface. For easy understanding, Fig. 11 shows the dependence of corrosion failure of the SS316L without and with a-C coating upon the operating temperature in PEMFCs for comparison.

4. Conclusion

In this work, we fabricated a-C coatings on SS316L substrate by a hybrid direct current magnetron sputtering system. The focus was dedicated into the dependence of electrochemical behavior and electrical conductivity of coatings upon solution temperature from 40° to 80° in a simulated PEMFC cathode environment. The microstructure evolution was comprehensively characterized by SEM and XPS, in order to identify the degradation mechanism of coatings before and after test. After the 24 h potentiostatic polarization tests, increasing the solution temperature led to the slight decrease of the corrosion resistance for coatings. However, noted that the stabilized maximum value of I_{corr} and the minimum conductivity of coating were only about 8.7 nA/cm^2 and coating 9.56 mΩ·cm^2, respectively, which were all well agreed within the standardization data of DOE 2025 (I_{corr} < 1 μA/cm^2, ICR < 10 mΩ·cm^2). The reason behind of this phenomenon could be mainly attributed to two aspects. First, the good chemical stability in a-C coating was achieved regardless of temperature variety, corresponding to the maintained sp^2/sp^3 atomic bonds. Nevertheless, due to the existence of growth defects like macroparticle and pinholes in a-C coatings by magnetron sputtering technique, increasing temperature distinctly accelerated the penetration of corrosive ions along the defects, resulting in the slight deterioration of a-C coating subsequently. An evident observation was that the elemental concentrations of released Fe and Cr ions became larger with temperature ascending, together with the stimulated damage of corrosion and conductivity in the coatings. In this case, the corrosion failure mechanism of a-C coated SS316L was suitably suggested in terms of operating temperature comparing with the performance of pristine SS316L for PEMFCs applications.

Supplementary data to this article can be found online at https://doi.org/10.1016/j.surfcoat.2024.130767.

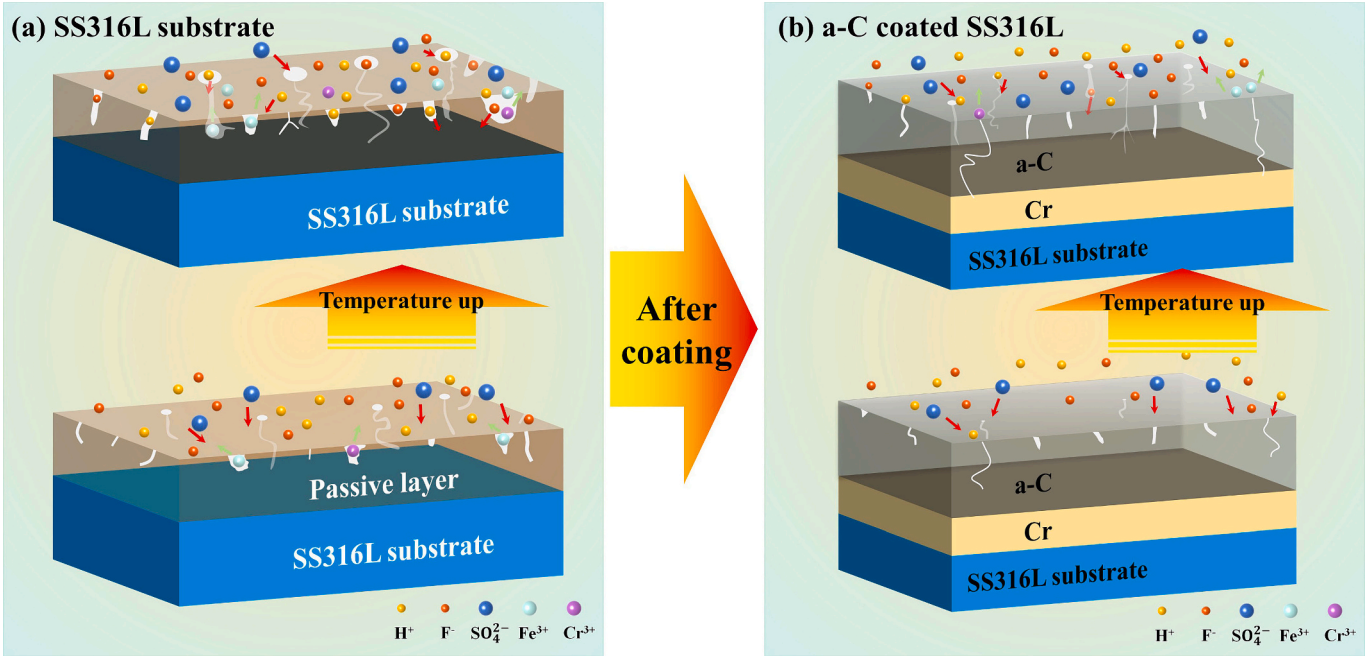

Fig. 11. Schematic image of the corrosion behavior of a-C coated SS316L in the simulated PEMFC cathode environment at different temperatures.

CRediT authorship contribution statement

Chao Jin: Writing – review & editing, Writing – original draft, Software, Methodology, Conceptualization, Data curation. **Peng Guo:** Conceptualization, Writing – review & editing, Supervision, Funding acquisition. **Hao Li:** Software, Methodology, Data curation, Conceptualization, Writing – review & editing. **Zhongyu Piao:** Supervision. **Keiji Komatsu:** Methodology. **Guanshui Ma:** Writing – review & editing, Data curation. **Rende Chen:** Supervision, Data curation. **Hidetoshi Saito:** Conceptualization. **Aiying Wang:** Writing – review & editing, Supervision, Methodology, Funding acquisition, Conceptualization.

Declaration of competing interest

The authors declare that they have no known competing financial interests or personal relationships that could have appeared to influence the work reported in this paper.

Data availability

The data that has been used is confidential.

Acknowledgment

This work was financially supported by National Science Fund for Distinguished Young Scholars of China (52025014), National Natural Science Foundation of China (U20A20296), Zhejiang Lingyan Research and Development Program (2022C01113), and Natural Science Foundation of Ningbo (2023J410).

References

[1] L. Fan, Z. Tu, S.H. Chan, Recent development of hydrogen and fuel cell technologies: a review, Energy Rep. 7 (2021) 8421–8446, https://doi.org/10.1016/j.egyr.2021.08.003.
[2] Z.-X. Yang, X.-G. Li, Q.-L. Yao, Z.-H. Lu, N. Zhang, J. Xia, K. Yang, Y.-Q. Wang, K. Zhang, H.-Z. Liu, L.-T. Zhang, H.-J. Lin, Q.-J. Zhou, F. Wang, Z.-M. Yu, J.-M. Ma, Roadmap on hydrogen energy from production to utilizations, Rare Metals 41 (2022) (2022) 3251–3267, https://doi.org/10.1007/s12598-022-02029-7.
[3] L. Fan, H. Deng, Y. Zhang, Q. Du, D.Y.C. Leung, Y. Wang, K. Jiao, Towards ultralow platinum loading proton exchange membrane fuel cells, Energy Environ. Sci. 16 (2023) 1466–1479, https://doi.org/10.1039/d2ee03169h.
[4] H. Li, H. Zhao, S. Jian, B. Tao, S. Gu, G. Xu, G. Wang, H. Chang, Designing proton exchange membrane fuel cells with high specific power density, J. Mater. Chem. A (2023), https://doi.org/10.1039/d3ta02545d.
[5] S. Karimi, N. Fraser, B. Roberts, F.R. Foulkes, A review of metallic bipolar plates for proton exchange membrane fuel cells: materials and fabrication methods, Adv. Mater. Sci. Eng. 2012 (2012) 1–22, https://doi.org/10.1155/2012/828070.
[6] Y. Song, C. Zhang, C.-Y. Ling, M. Han, R.-Y. Yong, D. Sun, J. Chen, Review on current research of materials, fabrication and application for bipolar plate in proton exchange membrane fuel cell, Int. J. Hydrog. Energy 45 (2020) 29832–29847, https://doi.org/10.1016/j.ijhydene.2019.07.231.
[7] P. Yi, D. Zhang, D. Qiu, L. Peng, X. Lai, Carbon-based coatings for metallic bipolar plates used in proton exchange membrane fuel cells, Int. J. Hydrog. Energy 44 (2019) 6813–6843, https://doi.org/10.1016/j.ijhydene.2019.01.176.
[8] R. Liu, Q. Jia, B. Zhang, Z. Lai, L. Chen, Protective coatings for metal bipolar plates of fuel cells: a review, Int. J. Hydrog. Energy 47 (2022) 22915–22937, https://doi.org/10.1016/j.ijhydene.2022.05.078.
[9] W. Li, L. Liu, Y. Wang, H. Li, Z. Li, Evaluation of vacuum heat-treated α-C films for surface protection of metal bipolar plates used in polymer electrolyte membrane fuel cells, Int. J. Hydrog. Energy 46 (2021) 22983–22997, https://doi.org/10.1016/j.ijhydene.2021.04.132.
[10] N. Konno, S. Mizuno, H. Nakaji, Y. Ishikawa, Development of compact and high-performance fuel cell stack, SAE International Journal of Alternative Powertrains 4 (2015) 123–129, https://doi.org/10.4271/2015-01-1175.
[11] M.-V. Müller, M. Giorgio, P. Hausmann, L. Kinlechner, A. Heinzel, J. Schwämmlein, Investigation of the effect of carbon post- vs pre-coated metallic bipolar plates for PEMFCs – start-up and shut-down, Int. J. Hydrog. Energy 47 (2022) 8532–8548, https://doi.org/10.1016/j.ijhydene.2021.12.179.
[12] D. Zhang, L. Peng, P. Yi, X. Lai, Electronic transport and corrosion mechanisms of graphite-like nanocrystalline carbon films used on metallic bipolar plates in proton-exchange membrane fuel cells, ACS Appl. Mater. Interfaces 13 (2021) 3825–3835, https://doi.org/10.1021/acsami.0c17764.
[13] B. Mi, H. Wang, Q. Wang, J. Cai, Z. Qin, Z. Chen, Corrosion resistance and contact resistance properties of Cr-doped amorphous carbon films deposited under different carbon target current on the 316L stainless steel bipolar plate for PEMFC, Vacuum 203 (2022), https://doi.org/10.1016/j.vacuum.2022.111263.
[14] Q. Meng, L. Yu, L. Shang, F. Wang, X. Liu, G. Zhang, Corrosive behavior and interfacial conductivity of stampable a-C film on titanium bipolar plate in proton exchange membrane fuel cells, Diam. Relat. Mater. 135 (2023), https://doi.org/10.1016/j.diamond.2023.109796.
[15] Q. Hu, J.-Y. Gao, S. Shu, Y.-X. Xu, J.-L. Luo, X.-Z. Wang, Corrosion behaviors of multilayer C/Cr/SS bipolar plates for proton exchange membrane fuel cells under dynamic potential polarization based on New European Driving Cycle, Corros. Sci. 214 (2023), https://doi.org/10.1016/j.corsci.2023.111032.
[16] J. Jin, X. Zhao, H. Liu, Durability and degradation of CrMoN coated SS316L in simulated PEMFCs environment: high potential polarization and electrochemical impedance spectroscopy (EIS), Int. J. Hydrog. Energy 44 (2019) 20293–20303, https://doi.org/10.1016/j.ijhydene.2019.05.169.
[17] F. Bi, X. Li, P. Yi, K. Hou, L. Peng, X. Lai, Characteristics of amorphous carbon films to resist high potential impact in PEMFCs bipolar plates for automotive application, Int. J. Hydrog. Energy 42 (2017) 14279–14289, https://doi.org/10.1016/j.ijhydene.2017.04.113.
[18] R. Tian, J. Sun, Effect of pH value on corrosion resistance and surface conductivity of plasma-nitrided 304L bipolar plate for PEMFC, Int. J. Energy Res. 35 (2011) 772–780, https://doi.org/10.1002/er.1737.
[19] J.j. Ma, J. Xu, S. Jiang, P. Munroe, Z.-H. Xie, Effects of pH value and temperature on the corrosion behavior of a Ta2N nanoceramic coating in simulated polymer electrolyte membrane fuel cell environment, Ceram. Int. 42 (2016) 16833–16851, https://doi.org/10.1016/j.ceramint.2016.07.175.
[20] J. Xuan, Y. Liu, L. Xu, S. Bai, Y. Xin, L. Wang, G. Zhang, Y. Su, L. Xue, L. Li, Investigation of acidity on corrosion behavior and surface properties of SS304 in simulated PEMFC cathode environments, Int. J. Hydrog. Energy 47 (2022) 22938–22951, https://doi.org/10.1016/j.ijhydene.2022.05.077.
[21] X.-Z. Wang, H. Luo, J.-L. Luo, Effects of hydrogen and stress on the electrochemical and passivation behaviour of 304 stainless steel in simulated PEMFC environment, Electrochim. Acta 293 (2019) 60–77, https://doi.org/10.1016/j.electacta.2018.10.028.
[22] M. Wilkinson, M. Blanco, E. Gu, J.J. Martin, D.P. Wilkinson, J.J. Zhang, H. Wang, In situ experimental technique for measurement of temperature and current distribution in proton exchange membrane fuel cells, Electrochem. Solid-State Lett. 9 (2006) A507, https://doi.org/10.1149/1.2338769.
[23] T. Fabian, R. O'Hayre, F.B. Prinz, J.G. Santiago, Measurement of temperature and reaction species in the cathode diffusion layer of a free-convection fuel cell, J. Electrochem. Soc. 154 (2007) B910, https://doi.org/10.1149/1.2752971.
[24] C.-Y. Wen, G.-W. Huang, Application of a thermally conductive pyrolytic graphite sheet to thermal management of a PEM fuel cell, J. Power Sources 178 (2008) 132–140, https://doi.org/10.1016/j.jpowsour.2007.12.040.
[25] Y. Yang, L. Guo, H. Liu, Factors affecting corrosion behavior of SS316L as bipolar plate material in PEMFC cathode environments, Int. J. Hydrog. Energy 37 (2012) 13822–13828, https://doi.org/10.1016/j.ijhydene.2012.04.026.
[26] J. Xuan, L. Xu, S. Bai, T. Zhao, Y. Xin, G. Zhang, L. Xue, L. Li, Influence of temperature on corrosion behavior, wettability, and surface conductivity of 304 stainless steel in simulated cathode environment of proton exchange membrane fuel cells, Int. J. Hydrog. Energy 46 (2021) 22920–22931, https://doi.org/10.1016/j.ijhydene.2021.04.119.
[27] H. Li, Y. Xin, K. Komatsu, P. Guo, G. Ma, P. Ke, K.-R. Lee, H. Saito, A. Wang, Controlling the compact- ness and sp2 clusters to reduce interfacial damage of amorphous carbon/316L bipolar plates in PEMFCs, Int. J. Hydrog. Energy 47 (2022) 11622–11632, https://doi.org/10.1016/j.ijhydene.2022.01.173.
[28] H. Li, P. Guo, D. Zhang, L. Liu, Z. Wang, G. Ma, Y. Xin, P. Ke, H. Saito, A. Wang, Interface-induced degradation of amorphous carbon films/stainless steel bipolar plates in proton exchange membrane fuel cells, J. Power Sources 469 (2020), https://doi.org/10.1016/j.jpowsour.2020.228269.
[29] I. Carvalho, N. Dias, M. Henriques, S. Calderon V, P. Ferreira, A. Cavaleiro, S. Carvalho, Antibacterial effects of bimetallic clusters incorporated in amorphous carbon for stent application, ACS Appl. Mater. Interfaces 12 (2020) 24555–24563, https://doi.org/10.1021/acsami.0c02821.
[30] J. Högström, M. Andersson, U. Jansson, F. Björefors, L. Nyholm, On the evaluation of corrosion resistances of amorphous chromium-carbon thin-films, Electrochim. Acta 122 (2014) 224–233, https://doi.org/10.1016/j.electacta.2013.11.130.
[31] D.D. Papadias, R.K. Ahluwalia, J.K. Thomson, H.M. Meyer, M.P. Brady, H. Wang, J. A. Turner, R. Mukundan, R. Borup, Degradation of SS316L bipolar plates in simulated fuel cell environment: corrosion rate, barrier film formation kinetics and contact resistance, J. Power Sources 273 (2015) 1237–1249, https://doi.org/10.1016/j.jpowsour.2014.02.053.
[32] X. Xiao, J. Zuo, Y. Wang, K. Wu, J. Zhang, G. Liu, J. Sun, Tuning the microstructure and mechanical properties in nanocrystalline Cr coatings by sputtering power, Mater. Sci. Eng. A 844 (2022), https://doi.org/10.1016/j.msea.2022.143204.
[33] Y. Liu, S. Li, H. Li, G. Ma, L. Sun, P. Guo, P. Ke, K.-R. Lee, A. Wang, Controllable defect engineering to enhance the corrosion resistance of Cr/GLC multilayered coating for deep-sea applications, Corros. Sci. 199 (2022), https://doi.org/10.1016/j.corsci.2022.110175.
[34] A.M.M. dos Santos, R.J.C. Batista, L.A.M. Martins, M. Ilha, M.Q. Vieira, D. R. Miquita, F.C.R. Guma, I.L. Müller, T.M. Manhabosco, Corrosion and cell viability studies of graphite-like hydrogenated amorphous carbon films deposited on bare and nitrided titanium alloy, Corros. Sci. 82 (2014) 297–303, https://doi.org/10.1016/j.corsci.2014.01.025.
[35] C.O.A. Olsson, D. Landolt, Passive films on stainless steels—chemistry, structure and growth, Electrochim. Acta 48 (2003) 1093–1104, https://doi.org/10.1016/s0013-4686(02)00841-1.

[36] F. Mansfeld, C.H. Tsai, Determination of coating deterioration with EIS: I, Basic relationships. Corrosion 47 (1991) 958–963.
[37] S. Ningshen, U. Kamachi Mudali, V.K. Mittal, H.S. Khatak, Semiconducting and passive film properties of nitrogen-containing type 316LN stainless steels, Corros. Sci. 49 (2007) 481–496, https://doi.org/10.1016/j.corsci.2006.05.041.
[38] S. Fujimoto, H. Tsuchiya, Semiconductor properties and protective role of passive films of iron base alloys, Corros. Sci. 49 (2007) 195–202, https://doi.org/10.1016/j.corsci.2006.05.020.
[39] L. Li, L.L. Liu, X. Li, P. Guo, P. Ke, A. Wang, Enhanced tribocorrosion performance of Cr/GLC multilayered films for marine protective application, ACS Appl. Mater. Interfaces 10 (2018) 13187–13198, https://doi.org/10.1021/acsami.8b00628.
[40] J. Xuan, Y. Xin, L. Xu, M. Guo, L. Huang, Y. Zhang, Y. Zhao, Y. Liu, L. Li, L. Xue, L. Li, Effects of fluoride ions on corrosion performance and surface properties of SS304 in simulated PEMFC cathodic environments, Renew. Energy 212 (2023) 769–778, https://doi.org/10.1016/j.renene.2023.05.117.
[41] Y. Yang, L.-j. Guo, H. Liu, Corrosion characteristics of SS316L as bipolar plate material in PEMFC cathode environments with different acidities, Int. J. Hydrog. Energy 36 (2011) 1654–1663, https://doi.org/10.1016/j.ijhydene.2010.10.067.
[42] Y. Yang, L. Guo, H. Liu, The effect of temperature on corrosion behavior of SS316L in the cathode environment of proton exchange membrane fuel cells, J. Power Sources 196 (2011) 5503–5510, https://doi.org/10.1016/j.jpowsour.2011.02.070.
[43] N.N. Khobragade, A.V. Bansod, A.P. Patil, Effect of dissolved oxygen on the corrosion behavior of 304 SS in 0.1 N nitric acid containing chloride, Materials Research Express 5 (2018) 046526, https://doi.org/10.1088/2053-1591/aab8de.
[44] D.G. Li, D.R. Chen, P. Liang, Influence of oxygen content on the corrosion behaviour of 316 L stainless steel in the simulated cathodic environment of proton exchange membrane fuel cell, J. Alloys Compd. 873 (2021) 159695, https://doi.org/10.1016/j.jallcom.2021.159695.
[45] D.D. Macdonald, The point defect model for the passive state, J. Electrochem. Soc. 139 (1992) 3434, https://doi.org/10.1149/1.2069096.
[46] Z. Cui, L. Wang, H. Ni, W. Hao, C. Man, S. Chen, X. Wang, Z. Liu, X. Li, Influence of temperature on the electrochemical and passivation behavior of 2507 super duplex stainless steel in simulated desulfurized flue gas condensates, Corros. Sci. 118 (2017) 31–48, https://doi.org/10.1016/j.corsci.2017.01.016.
[47] M. Kumagai, S.-T. Myung, S. Kuwata, R. Asaishi, H. Yashiro, Corrosion behavior of austenitic stainless steels as a function of pH for use as bipolar plates in polymer electrolyte membrane fuel cells, Electrochim. Acta 53 (2008) 4205–4212, https://doi.org/10.1016/j.electacta.2007.12.078.
[48] Y. Taki, O. Takai, XPS structural characterization of hydrogenated amorphous carbon thin films prepared by shielded arc ion plating, Thin Solid Films 316 (1998) 45–50, https://doi.org/10.1016/S0040-6090(98)00386-1.
[49] J. Díaz, G. Paolicelli, S. Ferrer, F. Comin, Separation of the sp^3 and sp^2 components in the C1s photo-emission spectra of amorphous carbon films, Phys. Rev. B 54 (1996) 8064–8069, https://doi.org/10.1103/PhysRevB.54.8064.
[50] P. Guo, X. Li, L. Sun, R. Chen, P. Ke, A. Wang, Stress reduction mechanism of diamond-like carbon films incorporated with different Cu contents, Thin Solid Films 640 (2017) 45–51, https://doi.org/10.1016/j.tsf.2017.09.001.
[51] F. Bi, K. Hou, P. Yi, L. Peng, X. Lai, Mechanisms of growth, properties and degradation of amorphous carbon films by closed field unbalanced magnetron sputtering on stainless steel bipolar plates for PEMFCs, Appl. Surf. Sci. 422 (2017) 921–931, https://doi.org/10.1016/j.apsusc.2017.06.122.
[52] Y. Liu, H. Du, X. Zuo, P. Guo, L. Liu, K.-R. Lee, A. Wang, P. Ke, Cr/GLC multilayered coating in simulated deep-sea environment: corrosion behavior and growth defect evolution, Corros. Sci. 188 (2021), https://doi.org/10.1016/j.corsci.2021.109528.
[53] Q. Li, Y. Zhang, Y. Cheng, X. Zuo, Y. Wang, X. Yuan, H. Huang, Effect of temperature on the corrosion behavior and corrosion resistance of copper-aluminum laminated composite plate, Materials (Basel) 15 (2022), https://doi.org/10.3390/ma15041621.
[54] H. Dai, S. Shi, L. Yang, C. Guo, X. Chen, Recent progress on the corrosion behavior of metallic materials in HF solution, Corros. Rev. 39 (2021) 313–337, https://doi.org/10.1515/corrrev-2020-0101.
[55] Z.B. Wang, H.X. Hu, Y.G. Zheng, Synergistic effects of fluoride and chloride on general corrosion behavior of AISI 316 stainless steel and pure titanium in H2SO4 solutions, Corros. Sci. 130 (2018) 203–217, https://doi.org/10.1016/j.corsci.2017.10.028.